nature communications

Article

https://doi.org/10.1038/s41467-025-57428-y

# A feedback circuitry involving γ-actin, β-actin and nonmuscle myosin-2 A controls tight junction and apical cortex mechanics

Received: 8 August 2024

Accepted: 21 February 2025

**Marine Maupérin [1], Yuze Sun [2], Thomas Glandorf [3], Tabea Anne Oswald [4], Niklas Klatt [3], Burkhard Geil [3], Annick Mutero-Maeda [1], Isabelle Méan [1], Lionel Jond [1], Andreas Janshoff [3], Jie Yan [2] & Sandra Citi [1]**

Cytoplasmic β- and γ-actin isoforms, along with non-muscle myosin 2 isoforms, are tightly regulated in epithelial cells and compose the actomyosin cytoskeleton at the apical junctional complex. However, their specific role in regulating the mechanics of the membrane cortex and the organization of junctions, and which biomechanical circuitries modulate their expression remain poorly understood. Here, we show that γ-actin depletion in MDCK and other epithelial cells results in increased expression and junctional accumulation of β-actin and increased tight junction membrane tortuosity, both dependent on nonmuscle myosin-2A upregulation. The knock-out of γ-actin also decreases apical membrane stiffness and increases dynamic exchange of the cytoplasmic tight junction proteins like ZO-1 and cingulin, without affecting tight junction organization and barrier function. In summary, our findings uncover a biomechanical circuitry linking γ-actin to β-actin expression through nonmuscle myosin-2A and reveal γ-actin as a key regulator of tight junction and apical membrane cortex mechanics, and the dynamics of cytoskeleton-associated tight junction proteins in epithelial cells.

The actomyosin cytoskeleton is composed of actin, myosin, and associated proteins, and is of primary importance in key cellular activities, such as adhesion, migration, cytokinesis, endocytosis, and maintenance of cell shape and mechanical homeostasis. In epithelial tissues, which are involved in protection, barrier, and polarized secretion and absorption functions, the actomyosin cytoskeleton contributes, among others, to the architecture, assembly and mechanical regulation of apical cell-cell junctions and to the maintenance of the tension and stiffness of the apical membrane cortex (reviewed in ref. 1–4). The apical cortex of epithelial cells also supports the assembly and function of actin-based structures such as microvilli and stereocilia[5,6] which are crucial for specialized tissue and organ functions, such as hearing[7]. Although epithelial cells express specific cytoplasmic actin and nonmuscle myosin isoforms, how each isoform fine-tunes the organization and function of cell-cell junctions and integrates mechanical forces to regulate junctional and apical membrane cortex mechanics is poorly understood. Moreover, the biomechanical circuitries that regulate the expression of and the crosstalk between specific actin and myosin isoforms and thus determine how cells respond to altered cytoskeletal composition and dynamics to maintain mechanical homeostasis is unclear.

Epithelial cells express two isoforms of cytoplasmic actin, γ-actin and β-actin, which differ by only four amino acids in their N-terminal sequences and display specific biochemical properties, localizations and functions (reviewed in ref. 8–11). For example, in MDCK kidney epithelial cells β-actin is localized at cell-cell junctions and along lateral membranes, while γ-actin is enriched at apical junctions and at the apical membrane cortex but is undetectable along lateral

---

[1]Department of Molecular and Cellular Biology, University of Geneva, Geneva, Switzerland. [2]Mechanobiology Institute, National University of Singapore, Singapore, Singapore. [3]Georg-August Universität, Institute for Physical Chemistry, Göttingen, Germany. [4]Georg-August Universität, Institute for Organic and Biomolecular Chemistry, Göttingen, Germany. e-mail: Sandra.Citi@unige.ch

membranes[12]. Although the molecular basis for these different localizations is unclear, knock-down (KD) and knock-out (KO) studies have addressed the specific roles of γ-actin and β-actin in a few types of cultured cells and in mouse tissues. In SK-CO15 human intestinal epithelial cells, siRNA-mediated depletion of either β-actin or γ-actin impairs the structure of either adherens junctions (AJs) or tight junctions (TJs), respectively, and attenuates the reassembly of both AJs and TJs[13]. Additional non-redundant roles of β-actin and γ-actin in cell motility, migration, angiogenesis and focal adhesion have been described in cultured endothelial and melanoma cancer cells[14,15]. In mice, the KO of β-actin leads to early embryonic lethality, whereas conditional KO of β-actin in the intestine results in increased permeability of the TJ intestinal barrier and exacerbation of colitis and inflammation[16]. In contrast, mice KO for γ-actin are viable, but show growth defects and progressive deafness[17,18], correlating with a specific pattern of stereocilia pathology, distinct from what is observed in mice with a conditional β-actin KO in hair cells[19]. Although compensatory up-regulation of β-actin upon depletion of γ-actin has been described both in in vitro and in vivo model systems[9,10,17,18], nothing is known on the mechanisms underlying such up-regulation. The contribution of actin isoforms to the regulation of junctional and apical membrane mechanics, which depend on forces generated by the actomyosin network[1,20,21], is also not known. The observation that β-actin predominantly resides in stress fibers and γ-actin is more typically found at the cell cortex and lamellipodia of migrating cells[12,22] suggests that actin networks formed predominantly by one or the other actin isoforms could provide membranes with different mechanical properties. Moreover, recent studies show that in vitro purified β-actin preferentially forms thin cable-like bundles, whereas purified γ-actin forms more organized interlinked mesh-like networks with distinct rheological properties[23]. However, it is not clear whether these different properties and localizations result in different mechanical properties of the membrane cortex within cells.

Force is generated by the interaction of actin filaments with myosins motors, and epithelial cells express three nonmuscle myosin-2 (NM2) isoforms: NM2A, NM2B and NM2C (reviewed in ref. 24–26). NM2A is widely expressed and is enriched in the peri-junctional circumferential actomyosin ring associated with apical junctions[27,28]. NM2B but not NM2A is detected in a juxta-membrane localization in assembling junctions, although NM2B also co-assembles with NM2A in the peri-junctional ring[29]. A role of NM2B in regulating TJ and apical membrane mechanics was postulated following the observation that the KO of cingulin, which recruits NM2B to TJs, results in decreased TJ membrane tortuosity and apical membrane stiffness in MDCK cells[30]. However, the KO of cingulin also resulted in reduced TJ proximity of γ-actin[30], suggesting that uncoupling γ-actin from TJs could also contribute to the mechanical phenotypes of cingulin-KO cells. To test this hypothesis, here we investigated the role of γ-actin in the organization and function of TJs, and TJ and apical membrane cortex mechanics, by generating clonal lines of γ-actin-KO MDCK cells, analyzing their phenotypes by biochemical, immunofluorescence microscopy, FRAP, and biophysical approaches, and confirming results by depletion, overexpression and rescue experiments in multiple epithelial cell types. In summary, here we show a regulatory feedback circuit whereby γ-actin controls β-actin expression and junctional accumulation by modulating NM2A expression and reveal new roles of γ-actin in the control of membrane cortex mechanics both at TJ and the apical membrane of epithelial cells.

## Results

### KO of γ-actin upregulates β-actin through increased NM2A expression

We used CRISPR/Cas9 technology and guides that targeted sequences within Exon 2 of the γ-actin gene to isolate three clonal lines of MDCKII cells (termed MDCK hereafter) KO for γ-actin, which contained distinct sequence deletions (clones #2H5, #2G3 and #3G9, Supplementary Fig. 1a). No expression of γ-actin was detected in any of the three clonal lines, based on immunoblot (IB) (Supplementary Fig. 1b) and immunofluorescence microscopy (IF) analyses (Supplementary Fig. 1c) of mixed cultures of WT and γ-actin-KO cells, using monoclonal antibodies specific for γ-actin[12]. Experiments carried out with each of the three different clonal lines gave essentially identical results.

We detected a significant increase in the signal for β-actin both at cell-cell junctions and in the cytoplasm of γ-actin-KO cells, compared to neighboring WT cells (double arrows in KO in Fig. 1a, top panel, quantification using PLEKHA6 as an internal junctional marker on the right). Labelling for β-actin was also increased in basal stress fibers of γ-actin-KO cells (double arrows in Supplementary Fig. 2a). In contrast, the labelling for phalloidin-labelled actin filaments was similar in WT and γ-actin KO cells both at junctions (single arrows in Fig. 1a, bottom panel, quantification on the right) and at basal stress fibers (single arrows in Supplementary Fig. 2b), suggesting similar amounts and contractility[30,31] of actin filaments. Correlating with increased immunofluorescent labelling for β-actin, we observed increased β-actin protein levels (IB in Fig. 1b, quantification in Fig. 1c), in agreement with previous data on γ-actin KO and KD cells[13,15,32], and increased β-actin mRNA levels (Supplementary Fig. 2c). Pan-actin protein levels were not affected, as determined by IB (Fig. 1b, quantification in Fig. 1c), in agreement with similar phalloidin labelling.

To confirm the specificity of the phenotype, we first rescued γ-actin-KO cells by re-expression of γ-actin, which was detected in transfected cells by IF at levels similar to WT (Supplementary Fig. 2d, compare to Fig. 1a), although total protein levels were low, due to the low efficiency of transfection (IB analysis in Supplementary Fig. 2e). Importantly, expression of exogenous γ-actin rescued the increase in β-actin detected in γ-actin KO cells (Supplementary Fig. 2d). Second, we depleted γ-actin from additional epithelial cell lines (mCCD, mouse collecting duct and Eph4, mouse mammary epithelium) by siRNA (Supplementary Fig. 2f-h) and we observed the same phenotype of increased β-actin expression (IB in Supplementary Fig. 2g, quantification in Supplementary Fig. 2h) and accumulation at junctions (Supplementary Fig. 2i, 2j, 2k for MDCK, mCCD and Eph4, respectively, quantifications on the right). In summary, the KO/depletion of γ-actin in epithelial cells results in an increase in junctional and cytoplasmic β-actin, without altering total actin levels.

Because of the different mechanical properties of β-actin and γ-actin filaments[23] and the different biochemical properties of nonmuscle myosins isoforms[24–26], we hypothesized that increased β-actin in γ-actin-KO cells could result in a feedback regulation of the expression and junctional localization of one or the other nonmuscle myosin isoforms. To test this idea, we carried out IF, IB and qRT-PCR analysis for NM2A and NM2B in γ-actin-KO versus WT MDCK cells. We observed that the junctional and cytoplasmic accumulation of NM2A was significantly increased in γ-actin-KO cells, compared to WT (double arrow, Fig. 1d, top panel, quantifications on the right), correlating with increased mRNA (Supplementary Fig. 3a) and protein expression levels (IB in Fig. 1e, quantification in Fig. 1f). In contrast, neither the junctional accumulation (Fig. 1d, bottom panel, quantification on the right) nor the protein expression levels of NM2B (Fig. 1e, quantification in Fig. 1f) were affected by the KO of γ-actin. Similar to what observed for β-actin, the up-regulation of NM2A was rescued by exogenous expression of γ-actin, as determined by IF analysis (Supplementary Fig. 3b, quantification on the right). Moreover, up-regulation of NM2A was observed upon depletion of γ-actin by siRNA both in MDCK cells and in additional epithelial cell lines (mCCD and Eph4), as determined by IB analysis (Supplementary Fig. 3d, quantification in Supplementary Fig. 3e) and by IF analysis (Supplementary Fig. 3f-h, quantifications on the right).

Next, we asked whether the increase in β-actin and NM2A were mechanistically linked. To test this idea, we depleted either NM2A or

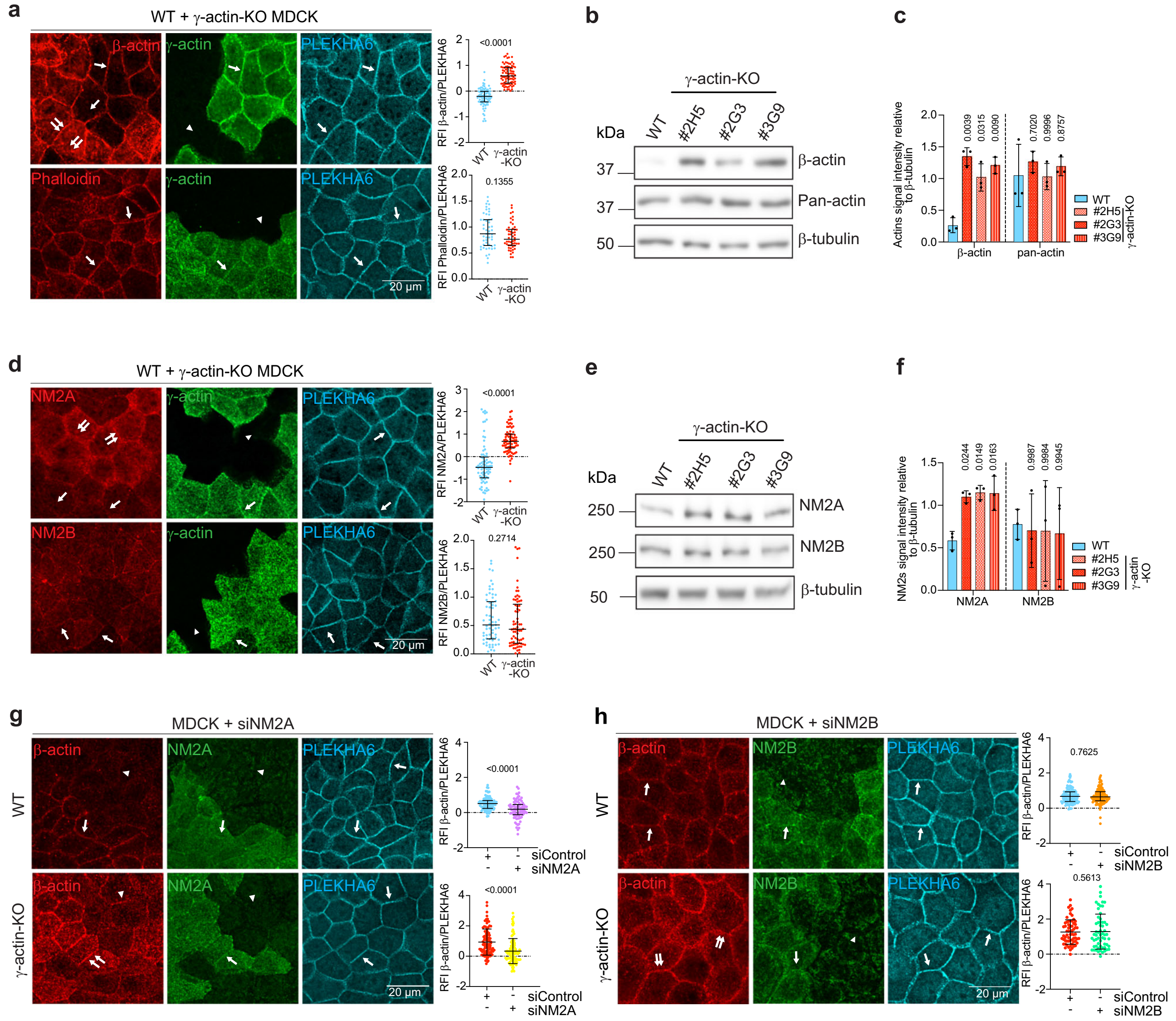

**Fig. 1 | γ-actin controls the expression and junctional accumulation of β-actin through NM2A. a, d** Immunofluorescence (IF) analysis and relative fluorescence intensity (RFI) quantifications (on the right of IF panels) of β-actin (top panels, increased, WT: *n* = 84, γ-actin-KO: *n* = 85) and phalloidin-labelled F-actin (bottom panels, not changed, WT and γ-actin-KO: *n* = 50 for) (**a**) NM2A (top panels, increased, WT: *n* = 82, γ-actin-KO: *n* = 78) and NM2B (bottom panels, not changed, WT: *n* = 65, γ-actin-KO: *n* = 70) (**d**) (red) at junctions in mixed cultures of WT (blue dots) and γ-actin-KO (red dots) distinguished via γ-actin (green), from 2 to 3 independent experiments. **b**, **c**, **e**, **f** Immunoblot (IB) analysis (**b**, **e**) and relative densitometric quantifications (**c**, **f**) of protein level of β-actin (increased) and pan-actin (not changed) (**b, c**) NM2A (increased) and NM2B (not changed) (**e, f**) in lysates of WT (blue dots) or γ-actin-KO (red dots) MDCK cells (3 distinct clonal lines) from 3 independent experiments. β-tubulin was used as a loading control. Dots shows replicates and bars represent mean ± SD. Indicated *p*-values are obtained from a two-sided one-way Anova test. **g** IF microscopy analysis and RFI quantifications of β-actin (red) at junctions in WT (top panels, siControl (blue dots): *n* = 85, siNM2A (purple dots): *n* = 83) or γ-actin-KO (bottom panels, siControl (red dots): *n* = 96, siNM2A (yellow dots): *n* = 93) cells upon NM2A depletion, distinguished via NM2A (green), from 3 independent experiments. Depletion of NM2A decreases β-actin localization. **h** IF microscopy analysis and RFI quantifications of β-actin (red) at junctions in WT (top panels, siControl (blue dots): *n* = 124, siNM2B (orange dots): *n* = 119) or γ-actin-KO (bottom panels, siControl (red dots): *n* = 63, siNM2B (green dots): *n* = 59) cells upon NM2B depletion, distinguished via NM2B (green), from 2-3 independent experiments. Depletion of NM2B does not alter β-actin localization. **a**, **d**, **g**, **h** Double arrows indicate increased β-actin or NM2A labelling. Arrows indicate normal β-actin, phalloidin, NM2A or NM2B labelling (as in WT cells). Arrowheads indicate loss of γ-actin or β-actin labelling in KO or KD cells, respectively. Scale bar = 20 μm. PLEKHA6 (cyan) is used as a junctional marker. Dots shows replicates and bars represent mean ± SD. Indicated p-values are obtained from a two-sided unpaired Mann-Whitney test. Source data for this figure are provided as a Source Data file.

NM2B (as negative control) in the context of either WT or γ-actin-KO cells and examined how this affected β-actin expression and localization. Treatment of MDCK cells with siRNA targeting either NM2A or NM2B resulted in a significant decrease in the respective protein levels (Supplementary Fig. 3i for NM2A, Supplementary Fig. 3j for NM2B, quantifications on the right). IF analysis showed that siRNA-mediated depletion of NM2A significantly decreased the junctional and cytoplasmic labelling for β-actin in both WT (arrowheads, Fig. 1g, top panels, quantifications on the right), and γ-actin-KO MDCK cells (arrowheads, Fig. 1g, bottom panels, quantifications on the right). This result was confirmed by the observation that depletion of NM2A in additional cell lines (mCCD and Eph4) also decreased the junctional accumulation of β-actin (Supplementary Fig. 3k-l). In contrast, the depletion of NM2B had no effect on the labelling for β-actin in either WT (Fig. 1h, top panels, quantifications on the right) or γ-actin-KO cells (Fig. 1h, bottom panels quantifications on the right).

In summary, the KO of γ-actin results in the increased expression and junctional accumulation of both β-actin and NM2A, and the levels of β-actin are controlled by NM2A.

## KO of γ-actin increases TJ tortuosity by up-regulating NM2A and β-actin

Previously we showed that in MDCK cells the KO of cingulin, which reduces the TJ proximity of γ-actin and the recruitment of NM2B to TJ, results in decreased TJ-membrane tortuosity and apical membrane stiffness[30]. To investigate the role of γ-actin in the regulation of junctional and apical membrane cortex mechanics, we first examined the effect of γ-actin-KO on TJ membrane tortuosity, expressed as zig-zag index[30,33]. In mixed cultures of WT and γ-actin-KO cells, TJ membrane tortuosity was significantly increased in γ-actin-KO cells compared to WT cells (Fig. 2a, quantifications on the right), and this increase in tortuosity was rescued by exogenous expression of γ-actin (Supplementary Fig. 4a, top panel, quantifications on the right) but not of GFP (Supplementary Fig. 4a, bottom panel, quantifications on the right). Moreover, the increase in tortuosity was also observed following siRNA-mediated depletion of γ-actin (Supplementary Fig. 4b, quantifications on the right), demonstrating that it is not a result of clone-specific variations.

To test whether the up-regulation of NM2A that we observed by IB and IF analysis (Fig. 1 and Supplementary Fig. 3) is mechanistically involved in the increased TJ membrane tortuosity of γ-actin-KO cells, we carried out siRNA-mediated depletion of either NM2A or NM2B in the background of either WT or γ-actin-KO cells (Supplementary Fig. 3i for NM2A, Supplementary Fig. 3j for NM2B, quantifications on the right). Depletion of NM2A significantly decreased the TJ membrane tortuosity both in WT cells (Fig. 2b, top panels, quantifications on the right) and γ-actin-KO cells (Fig. 2b, bottom panels, quantifications on the right). Conversely, depletion of NM2B had no effect on TJ membrane tortuosity either in WT (Fig. 2c, top panels, quantifications on the right) or γ-actin-KO cells (Fig. 2c, bottom panels quantifications on the right). To determine the contribution of β-actin to the tortuosity phenotype, we carried out transient siRNA-mediated depletion of β-actin in WT MDCK cells (Supplementary Fig. 4c). Depletion of β-actin resulted in a compensatory increase in junctional and cytoplasmic labelling for γ-actin and NM2A, (double arrows, Supplementary Fig. 4d), as well as an increase in their protein levels (Supplementary Fig. 4c). However, TJ membrane tortuosity was not significantly increased upon depletion of β-actin (Fig. 2d, quantification on the right), suggesting that the increase in TJ membrane tortuosity observed in γ-actin KO cells requires both NM2A and β-actin, and not only NM2A.

In summary, the KO of γ-actin promotes increased TJ membrane tortuosity through the increase in the expression and junctional accumulation of both NM2A and β-actin.

## KO of γ-actin reduces apical cortex stiffness and contractility

Although γ-actin accumulates at the apical cortex of polarized epithelial cells[12], nothing is known about the role of γ-actin in regulating the mechanical properties of the apical cortex. To address this question, we measured the local micro-elasticity and stiffness of the apical surface of WT and γ-actin-KO MDCK monolayers by atomic force microscopy (AFM). MDCK force-indentation curves were fitted by the Hertz model (Fig. 3a) to obtain the Young's modulus (Fig. 3b, Table 1). The average Young's modulus was significantly decreased in each of the three γ-actin-KO clonal lines, compared to WT (Fig. 3b, Table 1), and was rescued by exogenous expression of γ-actin (Fig. 3b, Table 1). Next, we compared the effect of KO of γ-actin to the effect of KO of cingulin. Using a different tension-based model that captures the viscoelastic properties of the cortex/membrane interface as well as the cortical tension due to the contractile action of the actomyosin[34,35], we observed a significant reduction in cortical tension, accompanied by a

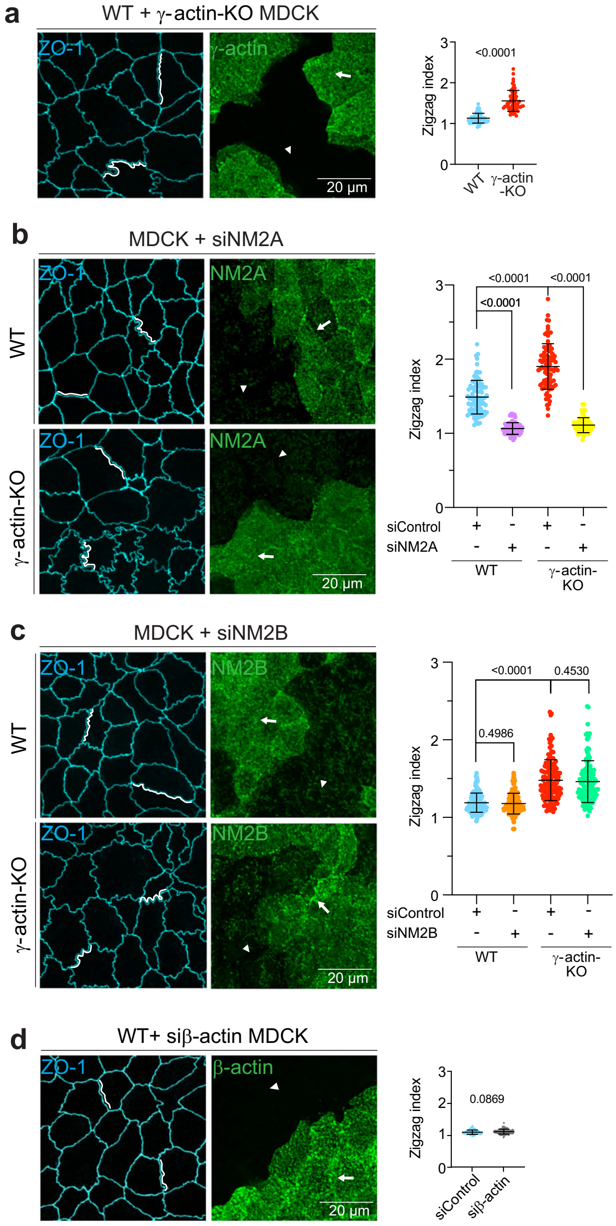

**Fig. 2 | γ-actin regulates TJ membrane tortuosity through NM2A. a** IF microscopy analysis and zigzag index quantifications (on the right of IF panels) of ZO-1 (cyan), used as a TJ marker, in mixed culture of WT (blue dots, *n* = 86) and γ-actin-KO (red dots, *n* = 87) cells distinguished via γ-actin (green), from 3 independent experiment. Tortuosity (zig-zag index) is increased in γ-actin-KO cells. **b** IF microscopy analysis and zigzag index quantifications of ZO-1 (cyan) in WT (top panels, siControl (blue dots): *n* = 90, siNM2A (purple dots): *n* = 88) or γ-actin-KO (bottom panels, siControl (red dots): *n* = 88, siNM2A (yellow dots): *n* = 83) cells upon NM2A depletion, distinguished via NM2A (green), from 3 independent experiments. Depletion of NM2A decreases tortuosity. **c** IF microscopy analysis and zigzag index quantifications of ZO-1 (cyan) in WT (top panels, siControl (blue dots): *n* = 143, siNM2B (orange dots): *n* = 141) or γ-actin-KO (bottom panels, siControl (red dots) and siNM2B (green dots): *n* = 128) cells upon NM2B depletion, distinguished via NM2B (green), from 3 independent experiments. Depletion of NM2B does not alter tortuosity. **d** IF microscopy analysis and zigzag index quantifications of ZO-1 (cyan) in WT cells upon β-actin depletion (siControl (blue dots) and siβ-actin (grey dots): *n* = 90), distinguished via β-actin (green), from 3 independent experiments. Depletion of β-actin does not alter tortuosity. **a**–**d** The white line represents the TJ-membrane tortuosity. Scale bar = 20 µm. Dots shows replicates and bars represent mean ± SD. Indicated p-values are obtained from a two-sided unpaired Mann-Whitney test. Source data for this figure are provided as a Source Data file.

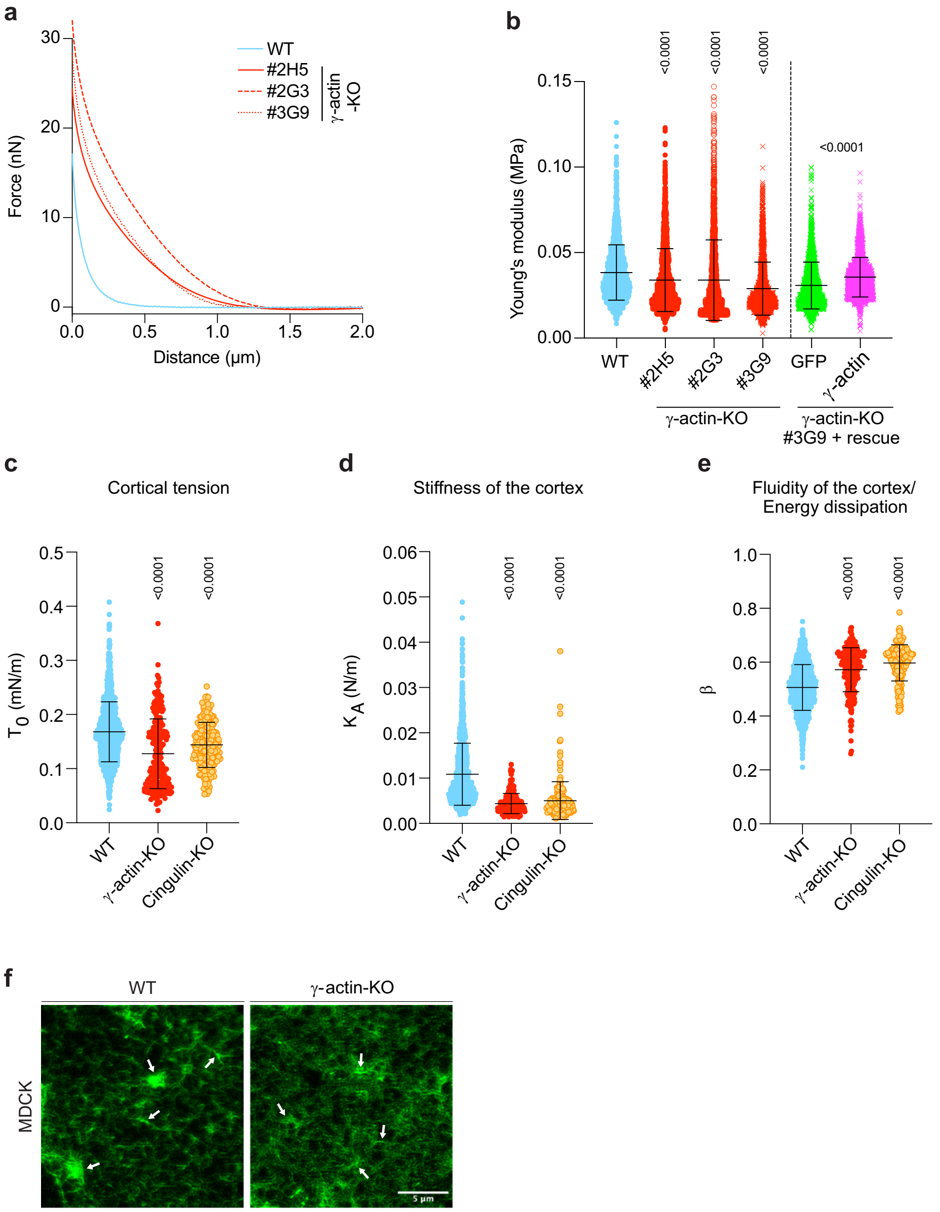

**Fig. 3 | γ-actin regulates apical membrane cortex mechanics. a** Representative AFM force-indentation curves of WT and γ-actin-KO (3 distinct clonal lines) MDCK cells fitted with Hertz (Spherical) model. **b** Average stiffness (Young's modulus) of WT (blue dots, $n = 2186$), γ-actin-KO (3 distinct clonal lines) (red dots, #2G3 and #2H5: $n = 2067$, #3G9: $n = 1999$), γ-actin-KO rescued with either GFP as a control (green dots, $n = 1896$) or by full-length canis γ-actin (γ-actin) (pink dots, $n = 2052$) MDCK cells from 3 independent experiments. The Young's modulus is decreased in γ-actin-KO cells. **c**–**e** Results from fitting the three parameters, cortical tension (prestress, $T_0$), area compressibility modulus (scaling factor, $K_A{}^0$) and fluidity (β) of the tension-based model (Eq. (2)) to the experimental indentation-relaxation data of confluent cells (WT (blue dots): $n = 1152$, γ-actin-KO (red dots): $n = 243$, cingulin-KO (orange dots): $n = 167$) from 3 independent experiments. **b**–**e** Dots shows replicates and bars represent mean ± SD. Indicated p-values are obtained from a two-sided unpaired Mann-Whitney test. Cortical tension and stiffness are decreased and fluidity is increased in γ-actin-KO cells. **f** Representative STED images of isolated apical cortices of WT and γ-actin-KO MDCK cells. Scale bar = 5 µm. Arrows indicate contraction foci, which were smaller and less intensely labelled in γ-actin-KO cells. Source data for this figure are provided as a Source Data file.

decrease of stiffness (area compressibility modulus, $K_A^0$) (Fig. 3c-d) concomitant with an increase in fluidity (β) (Fig. 3e, Table 2). This effect resembles the administration of an actin-severing drug such as latrunculin[34].

To correlate the mechanical properties of cells with their cortical architecture, we prepared apical cortices from living MDCK cells using the sandwich cleavage method[36]. STED microscopy analysis revealed that cortices from WT and γ-actin-KO cells both form a mesh-like network, with virtually identical mesh sizes. Using bubble analysis[37], we measured mesh sizes of 125 ± 60 nm for WT cells and 118 ± 52 nm for γ-actin-KO cells. Interestingly, WT cortices show contraction foci, which we attribute to local collapse of the network in response to high motor activity, that appeared more intensely labelled compared to γ-actin-KO cells (arrows in Fig. 3f). The morphology of the contraction foci is likely reflected in our mechanical measurements, as the tension ($T_0$) is higher in WT cells compared to γ-actin-KO cells.

Together, these results indicate that γ-actin is required to maintain a contractile, organized and stiffer apical cortex in MDCK cells, and that the KO of either γ-actin or cingulin has similar effects on the stiffness, contractility and fluidity of the apical cortex.

Table 1 | Young's modulus values of WT, γ-actin-KO, γ-actin-KO rescued with either γ-actin or GFP in MDCK cells (Fig. 3a-b)

| Line genotype | Young's modulus (MPa) |
|---|---|
| WT | 0.03835 ± 0.01620 |
| γ-actin-KO #2G3 | 0.03388 ± 0.01837 |
| γ-actin-KO #2H5 | 0.03364 ± 0.02303 |
| γ-actin-KO #3G9 | 0.02891 ± 0.01547 |
| γ-actin-KO #3G9 rescued with GFP control | 0.03076 ± 0.01366 |
| γ-actin-KO #3G9 rescued with γ-actin | 0.03566 ± 0.01155 |

Table 2 | Values (mean ± standard deviation) of viscoelastic parameters obtained from fitting indentation relaxation curves on WT, γ-actin-KO, and cingulin-KO MDCK cells (Fig. 3c-e)

| Line genotype | $T_0$ (mN/m) | $K_A{}^0$ (N/m) | β |
|---|---|---|---|
| WT | 0.17 ± 0.06 | 0.011 ± 0.007 | 0.51 ± 0.09 |
| γ-actin-KO #3G9 | 0.13 ± 0.06 | 0.004 ± 0.002 | 0.57 ± 0.08 |
| Cingulin-KO #1G8 | 0.14 ± 0.04 | 0.005 ± 0.004 | 0.60 ± 0.07 |

### KO of γ-actin promotes increased ZO-1 and cingulin exchange

In SK-CO15 cells depletion of γ-actin in MDCK cells affects TJ organization and TJ barrier function[13]. To examine whether KO of γ-actin affects TJs and AJs in MDCK cells, we carried out IF and IB analysis, and studied TJ barrier function in our KO lines. The localization and intensity of IF labelling of cytoplasmic and transmembrane proteins of TJ, namely ZO-1, cingulin and occludin was indistinguishable when comparing confluent WT and γ-actin-KO MDCK cells in mixed cultures (Fig. 4a). In addition, the measurement of transepithelial electrical resistance (TEER) (Fig. 4b) and permeability to 3-kDa dextran (Fig. 4c) of confluent MDCK monolayers was not significantly different when comparing WT cells and each of the three clonal KO lines. Finally, IB analysis of the protein expression levels of ZO-1, cingulin and occludin (Supplementary Fig. 5a, quantification in Supplementary Fig. 5b) and claudins-1, -2, -3, -4, -7, -8, -10 (Supplementary Fig. 5c, quantification in Supplementary Fig. 5d) showed no significant difference in the expression of these TJ proteins when comparing WT cells and γ-actin KO clonal lines. Moreover, we found no evidence for altered localization (arrows in Supplementary Fig. 5e) and expression (Supplementary Fig. 5f, quantification in Supplementary Fig. 5g) of the AJ proteins afadin, E-cadherin and β-catenin. Thus, γ-actin-KO MDCK cells display normal organization of TJ and AJ and normal TJ barrier function.

Since the actomyosin cytoskeleton regulates the dynamic exchange between junction-associated and cytoplasmic pools of TJ proteins[38,39], we hypothesized that the loss of γ-actin could alter such dynamics, and hence the exchange of ZO-1 and cingulin. To address this question, we performed fluorescence recovery after photobleaching (FRAP) experiments on either overexpressed GFP-tagged cingulin or GFP-tagged ZO-1, in the context of either WT or γ-actin-KO MDCK cells. The dynamic behaviors of cingulin and ZO-1 in WT cells were similar to what was previously reported[38–40], e.g. the mobile fractions were 68% for cingulin and 49% for ZO-1 (blue traces Fig. 4e for cingulin and Fig. 4i for ZO-1) whereas the half-times were 80 sec for cingulin and 96 sec for ZO-1 (blue traces Fig. 4f for cingulin and Fig. 4j for ZO-1, respective kymographs in Figs. 4g and 4k, top panels, live imaging in Supplementary Movies 1 and 3). In addition, mobile fractions of both cingulin and ZO-1 were significantly higher and the half-times were significantly lower in γ-actin-KO cells, e.g. the mobile fraction was 76% for cingulin and 60% for ZO-1, and the half-time was 48 sec for cingulin and 59 sec for ZO-1 (red traces in Fig. 4d-f for cingulin and Fig. 4h-j for ZO-1, respective kymographs in Figs. 4g and 4k, bottom panels, live imaging in Supplementary Movies 2 and 4). Since myosin activity was reported to affect ZO-1 exchange[39], we asked whether this is the case also in the background of γ-actin-KO cells. FRAP analysis showed that blebbistatin, which inhibits myosin-2 activity[31] slowed down the recovery of ZO-1 in γ-actin-KO compared to DMSO (Fig. 4i), e.g. the mobile fractions were 76% for DMSO (red trace Fig. 4m) and 54% for blebbistatin (pink trace Fig. 4m), whereas the half-times were 68 sec for DMSO (red trace Fig. 4n) and 53 sec for blebbistatin (pink trace Fig. 4n, respective kymographs in Fig. 4o, live imaging in Supplementary Movies 5 and 6).

In summary, the KO of γ-actin results in increased dynamic exchange of cingulin and ZO-1, suggesting that both γ-actin and myosin-2 activity control the dynamics of cytoplasmic proteins of TJs.

## Discussion

The architecture and function of junctions, and the mechanics of the plasma membrane cortex depend on the organization, dynamics and contractility of the actomyosin cytoskeleton. Here we identify a biomechanical circuitry, whereby the KO of γ-actin results in NM2A-dependent up-regulation of β-actin, and the up-regulation of both NM2A and β-actin increases in turn TJ membrane tortuosity. We also show that the KO of γ-actin reduces apical membrane cortex stiffness, and affects the dynamics of TJ proteins, but not TJ organization and barrier function in MDCK epithelial cells.

Little is known about the specific functions of actin isoforms and the mechanisms of regulation of their expression. Early transfection studies showing reciprocal feedbacks between expression of cytoplasmic actin isoforms[41–43] were confirmed by the observation that depletion of γ-actin results in "compensatory" up-regulation of β-actin in cultured cells and mouse tissues[13,15,17]. Our rescue experiments and analysis of multiple cell types strongly support a major role of increased NM2A in regulating β-actin levels in γ-actin-depleted epithelial cells, suggesting a biomechanical feedback circuitry. The transcriptional and/or translational mechanisms through which NM2A and β-actin are up-regulated are beyond the scope of this study and remain to be investigated. However, changes in cytoskeletal organization and dynamics are known to affect signaling cascades that regulate gene expression, through transcription factors such as MRTF, SRF and YAP[44–47] (reviewed in ref. 48,49). For example, depletion of γ-actin in A549 lung cancer cells activates SRF and MRTF transcription factors to induce the expression of myofibroblast markers such as smooth muscle actin[50]. Since SRF has been implicated in the up-regulation of the gene coding for NM2A (MYH9), resulting in a matching translational response[51], we hypothesize that SRF is implicated in the increased expression of NM2A observed in γ-actin-KO cells.

In a previous study, depletion of γ-actin in SK-CO15 epithelial cells did not affect protein levels of NM2A, NM2B, NM2C, but only caused a decrease in phosphorylated myosin light chain[13]. No effect on myosin was observed in γ-actin-KO melanoma cells[15]. Therefore, the effects of depletion of γ-actin on the expression of NM2 may somewhat depend on the cellular context. However, considering the different rheological and mechanical properties of actin filaments made of either β-actin or γ-actin[23] and their different rate of polymerization[52], it is likely that cells can sense changes induced by the absence of γ-actin and respond by changing the levels expression of actin and myosin isoforms. Indeed, our results indicate the existence of a biomechanical sensing mechanism, whereby the absence of γ-actin entails an up-regulation of mRNA and protein levels for NM2A, which, in turn, induce the up-regulation of β-actin. Since NM2A does not appear to exhibit a preferential binding affinity for either actin isoform[53], it appears unlikely that the increase in β-actin is due to its stabilization through interaction with NM2A.

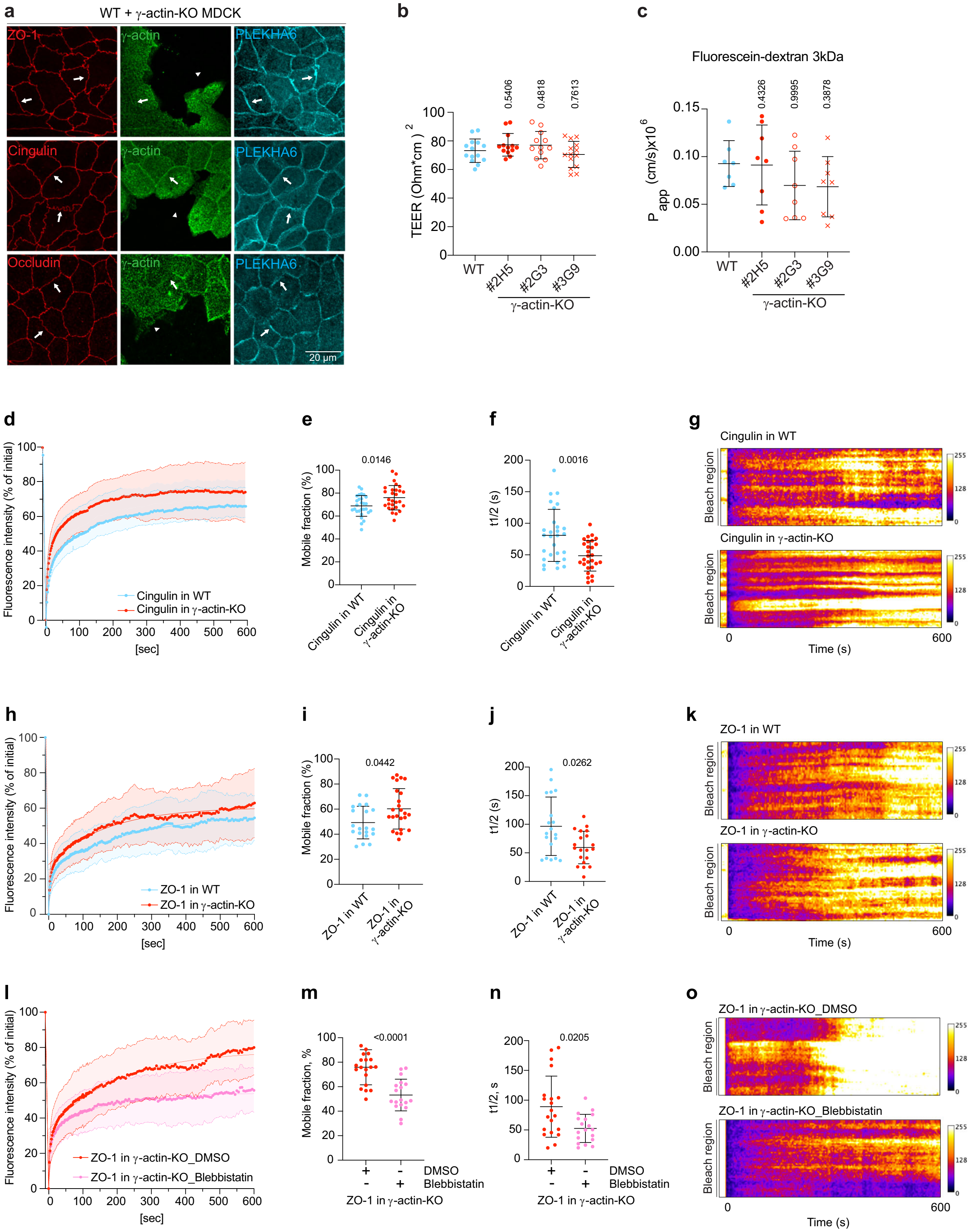

Ultimately, the correct combination and spatial organization of specific myosin and actin isoforms control membrane cortex mechanics. The KO of γ-actin in MDCK cells resulted in two distinct mechanical phenotypes: increased TJ-membrane tortuosity and decreased stiffness of the apical plasma membrane. TJ-membrane tortuosity is the result of orthogonal forces generated by the contractility of the circumferential actomyosin bundle associated with apical junctions[3,21,54]. As such, it is regulated by different proteins directly or indirectly associated with the actomyosin cytoskeleton, including ZO-1[33,55], Shroom[56], Lulu[57], cingulin[30] and other factors (reviewed in ref. 58). Importantly, TJ-membrane tortuosity is reduced by the inhibitor blebbistatin, which acts primarily on NM2A[30,31,33,55]. Here we show, in agreement, that depletion of NM2A decreases TJ-membrane tortuosity in WT and γ-actin-KO MDCK cells, indicating that

**Fig. 4 | KO of γ-actin increases the junctional dynamics of cingulin and ZO-1. a** IF analysis of the localization of ZO-1, cingulin and occludin (not changed, red) in mixed cultures of WT and γ-actin-KO cells distinguished via γ-actin (green), from 3 independent experiments. PLEKHA6 (cyan) is used as a junctional reference marker. Scale bar = 20 μm. **b** Transepithelial electrical resistance (TEER) measurement of WT (blue dots, n = 14) and γ-actin-KO (red dots, 3 distinct clonal lines: #2G3: *n* = 13, #2H5: *n* = 12, #3G9: n = 14) MDCK at steady-state from 5 independent experiments. The KO of γ-actin does not alter the TEER. **c** Paracellular permeability ($P_{app}$) to 3 kDa fluorescein-dextran measurement of WT (blue dots, n = 7) and γ-actin-KO (red dots, 3 distinct clonal lines: *n* = 8) MDCK from 3 independent experiments. The KO of γ-actin does not alter the $P_{app}$. **b, c** Dots shows replicates and bars represent mean ± SD. Indicated p-values are obtained from a two-sided one-way Anova test. **d–k** Quantitative FRAP analysis (**d, h**), mobile fraction (**e, i**), half-time ($t_{1/2}$) (**f, j**) and representative kymographs (**g, k**) for GFP-cingulin-FL (**d–g**) or GFP-ZO-1-FL (**h–k**) overexpressed in WT (blue dots, cingulin: *n* = 28, ZO-1: n = 21 for mobile fraction and n = 19 for $t_{1/2}$) or γ-actin-KO (red dots, cingulin: *n* = 28, ZO-1: n = 22 for mobile fraction and n = 20 for $t_{1/2}$) MDCK cells from 3 independent experiments. The exchange of cingulin and ZO-1 is increased in γ-actin-KO cells. **l–o** Quantitative FRAP analysis (**l**), mobile fraction (**m**), $t_{1/2}$ (**n**) and representative kymographs (**o**) for GFP-ZO-1-FL overexpressed in γ-actin-KO MDCK cells treated with either DMSO (red dots, *n* = 20) or blebbistatin (pink dots, n = 18) from 3 independent experiments. The exchange of ZO-1 is inhibited by blebbistatin. **d–o** Related Supplementary Movies 1, 2, 3, 4, 5 and 6 show FRAP live imaging of GFP-cingulin-FL in WT (Suppl. Movie 1) and γ-actin-KO (Suppl. Movie 2), or GFP-ZO-1-FL in WT (Suppl. Movie 3) and in γ-actin-KO (Suppl. Movie 4) MDCK cells, or GFP-ZO-1-FL in γ-actin-KO MDCK cells treated with DMSO (Suppl. Movie 5) or blebbistatin (Suppl. Movie 6). Indicated p-values are obtained from a two-sided unpaired T-test. Source data for this figure are provided as a Source Data file.

the increased TJ-membrane tortuosity of γ-actin-KO cells is the direct consequence of increased NM2A expression. The observation that increased NM2A expression in β-actin-depleted cells did not result in increased tortuosity suggests that γ-actin cannot functionally replace β-actin with regards to the generation and transmission of force from the circumferential belt to the TJ membrane. Finally, the observation that depletion of NM2B does not affect TJ-membrane tortuosity suggests that the decreased TJ-membrane tortuosity detected in cingulin-KO MDCK cells is likely not due to decreased junctional recruitment of NM2B, as previously proposed[30], but rather to the disruption of the integrity the cingulin-ZO-1-actomyosin complex, which works as a mechano-transduction linker module between the AJC-associated circumferential actomyosin belt and the TJ[54].

The reduction in apical membrane stiffness detected in γ-actin-KO cells was quantitatively very similar to that observed in cingulin-KO MDCK cells, where TJ proximity of γ-actin was decreased[30]. This suggests that cingulin regulates apical membrane stiffness by uncoupling γ-actin from the TJ. It was also recently reported that depletion of ZO-2 in MDCK cells results in reduced junctional association of γ-actin, correlating with decreased apical membrane stiffness[59]. Taken together, these observations indicate that the anchoring of γ-actin filaments to TJ is maintained by non-redundant interactions with ZO proteins-cingulin TJ complexes and determines apical membrane stiffness. We propose that γ-actin provides the apical membrane with increased stiffness through its ability to generate a stronger, stiffer meshwork of filaments, when compared to meshwork of β-actin filaments[23]. Importantly, apical membrane stiffness is critical for auditory function, and γ-actin-KO mice show altered architecture of stereocilia of hair cells and progressive hearing loss[17,19,60]. A stiffer cortex may be required to counter the mechanical stimulation to which hair cells are continuously exposed. Intriguingly, either KO or mutation of cingulin in mice and humans is associated with progressive hearing loss, through increased death and apoptosis of hair cells[61]. Our results suggest that cingulin and γ-actin control survival of hair cells and hearing function by maintaining apical membrane stiffness and cellular integrity upon mechanical stress, through their ability to anchor γ-actin and NM2B to TJs (cingulin) and provide the cortex with specific biophysical stiffness properties (γ-actin). Other mechanisms have been described through which TJ proteins can affect hearing, such as increased apoptosis induced by overexpression of ZO-2[62] and altered TJ-dependent ionic permeability resulting from loss or mutations of claudins[63–65], tricellulin[65], and occludin[66]. However, such a mechanism is unlikely for cingulin and γ-actin, since there is insufficient evidence for a significant effect of their KO on barrier function of epithelial cells[67–69].

At variance with a previous report[13], we found no effect of the depletion of γ-actin on the molecular organization of TJ and AJ, and the barrier function of TJ. This discrepancy may be due to different cell types, methods of depletion, and state of assembly of junctions. Our finding that TJs were not affected by KO of γ-actin is consistent with the observation that in the mouse KO of γ-actin, unlike the KO of β-actin, does not affect viability of the mouse and the formation of epithelial organs[17–19], indicating normal organization and function of the apical junctional complex and normal TJ barrier function. Interestingly, despite unchanged TJ organization and barrier function in γ-actin-KO MDCK cells, we observed increased dynamic exchange of cingulin and ZO-1 at TJ. Previously, it was shown that both MLCK-dependent and MLCK-independent processes regulate the exchange of ZO-1 at TJs. Although MLCK inhibition profoundly reduces ZO-1 exchange, a ZO-1 mutant lacking the actin-binding region remains sensitive to actomyosin disruption[39]. Thus, the connection of ZO-1 to the actomyosin cytoskeleton through the ZU5-mediated anchoring to the cingulin-NM2B complex[30] may represent an additional mechanism of regulation of ZO-1 dynamics[70]. Our FRAP results and the effect of blebbistatin suggest that increased levels of NM2A increase the dynamic exchange of cytoplasmic TJ proteins such as ZO-1 and cingulin in γ-actin-KO cells. However, we cannot exclude other possibilities, including differences in the dynamics of β-actin and γ-actin filaments[52], and different affinities of interaction of β-actin versus γ-actin filaments with the ZO-1-cingulin complex. Future work should clarify whether the juxtamembrane branched actin network[29] is made primarily of γ-actin and to determine whether actin-binding proteins of the TJ[55,71–74] show different affinity for γ-actin versus β-actin filaments.

In summary, through KO, KD and rescue experiments in MDCK, mCCD and EpH4 cells we uncover a role for γ-actin in a mechanosensitive circuitry that controls the expression of NM2A and β-actin and regulates membrane cortex mechanics and cytoplasmic TJ protein dynamics.

# Methods

## Genome engineering

γ-actin-KO cells were generated in the canine MDCKII (MDCK) cell line (MDCK TetOff, a kind gift from Alan Fanning, Univ. North Carolina) by CRISPR/Cas9 gene editing technology. The target sequences were designed using the Genscript guide RNA (gRNA) designing tool and selected to target in exon 2 (Supplementary Fig. 1). The gRNAs were subcloned into the BbsI site of the pSpCas9(BB)-2A-GFP (PX458) CRISPR plasmid, and transfected in MDCK WT cells using JetOptimus (Polyplus, #101000051). 48 hr post-transfection, GFP-positive single-cell were sorted by a Beckman Coulter MoFlo Astrios sorter (Flow Cytometry Platform, Geneva Medical School) and transferred into 96-well tissue culture plates containing conditioned media from WT MDCK. Single clones were amplified and screened for KO by immunoblot (IB) and immunofluorescence (IF) microscopy analysis. For sequencing, genomic DNA was extracted using DNeasy Blood and Tissue kit (Qiagen, #69504). The genomic locus surrounding the target region was amplified by PCR using forward primer For_gaggaggcggccgcCATGGACTCTGGGGATGGC and reverse primer Rev_gaggaattcCTTGCGTTCCGGAGGAGCAA. To separate the alleles before being sequencing, purified PCR products were subcloned into pBluescript II KS (+) using NotI and EcoRI as restriction enzymes. The M13 primer was used for sequencing the inserts for genotyping. 3 clones of γ-actin-KO were generated: clone #2G3, clone #2H5, clone #3G9.

### Experimental model

MDCK (Madin-Darby Canine Kidney type II cell line, female, Tet-off), mCCD (mouse cortical collecting duct epithelial line) and EpH4 (mouse mammary epithelial cell line, female) (Supplementary Table 1) were cultured in Dulbecco's Modified Eagle's (DMEM) medium supplemented with 10% or 20% (for mCCD) Fetal Bovine Serum (FBS), 1% non-essential aminoacids (NEAA), 100 units/mL penicillin and 100 μg/mL streptomycin (P/S) (standard medium), at 37 °C, under 5% of $CO_2$[69]. Rescue stable cell lines were generated by transfecting γ-actin-KO clone #3G9 with either full-length γ-actin or GFP alone using JetOptimus DNA transfection reagent (Polyplus, #117-15). 48 hr post-transfection, single cells were sorted into 96-well tissue culture plates using a Beckman Coulter MoFlo Astrios sorter (Flow Cytometry Service, University of Geneva Medical School). Individual clones were then screened through IB and IF analysis, and their phenotypes were validated in 2-3 distinct clonal lines.

### Plasmids

Constructs of GFP-cingulin-FL in pTRE2Hyg[75], GFP-myc in pTRE2Hyg[76], GFP-ZO-1-FL in pTRE2Hyg[70] were described previously. Additional plasmids are described in Supplementary Table 1.

Full-length canis γ-actin (1-375 aa, S2882) was synthesized by Genscript (https://www.genscript.com/gene_synthesis.html), amplified by PCR with the appropriate oligonucleotides and subcloned into the pTRE2Hyg plasmid under the control of a 3 kb human β-actin promoter (a gift from Prof. Bernhard Wehrle-Haller (Geneva Medical School, Switzerland)[77]) using the restriction sites SpeI and EcoRV. Full-length canis β-actin (1-375 aa, S2926) was obtained by mutating the full-length canis γ-actin (1-375 aa, S2882) at positions 2, 3, 4, 10 (E2D, E3D, E4D, I10V). All constructs were validated by sequencing (Microsynth, Switzerland).

### Antibodies

The primary antibodies targeting the indicated proteins, along with their host species, were used at the following dilution for immunoblotting (IB) and immunofluorescence (IF): mouse IgG2b γ-actin (2A368E2, Prof. Christine Chaponnier (Geneva Medical School, Switzerland)[12], IB: 1/500, IF: 1/200), mouse IgG1 β-actin (4C259H12, Prof. Christine Chaponnier (Geneva Medical School, Switzerland)[12], IB: 1/1 000, IF: 1/200), rat PLEKHA6 (RtSZR127, IF: 1/100)[78], guinea pig PLEKHA7 (GP2737, IF: 1/300)[78], rabbit NM2A (909801, Biolegend, IB: 1/1 000, IF: 1/200), rabbit NM2B (909901, Biolegend, IB: 1/1 000, IF: 1/200), mouse GFP (11814460001, Roche, IF: 1/100), mouse β-tubulin (32-2600, Thermo Fisher Scientific, IB: 1/2 500), mouse pan-actin (mab1501, Sigma, IB: 1/1 000), rat ZO-1 (R4076, from Prof. Daniel Goodenough (Harvard Medical School, USA), IF: 1/100), mouse ZO-1 (3391000, Thermo Fisher Scientific, IB: 1/1 000), rabbit cingulin (C532, Citi Lab, IB: 1/5 000, IF: 1/5 000), mouse E-cadherin (BD610181, BD Biosciences, IB: 1/5 000), rabbit E-cadherin (7870, Santa Cruz, IF: 1/100), rabbit β-catenin (C2206, Sigma, IF: 1/500, IB: 1/5 000), rabbit Claudin-1 (51-9000, Thermo Fisher Scientific, IB: 1/500), mouse Claudin-2 (32-5600, Thermo Fisher Scientific, IB: 1/500), rabbit Claudin-3 (34-1700, Thermo Fisher Scientific, IB: 1/500), mouse Claudin-4 (32-9400, Thermo Fisher Scientific, IB: 1/500), rabbit Claudin-7 (34-9100, Thermo Fisher Scientific, IB: 1/500), mouse Claudin-8 (40-0700Z, Thermo Fisher Scientific, IB: 1/500), mouse Claudin-10 (38-8400, Thermo Fisher Scientific, IB: 1/500). The specificity of the anti-myosin antibodies has been validated previously[30].

Secondary antibodies used for IB were: anti-mouse IgG HRP (H + L) conjugate (W4021, Promega, IB: 1/4 000), anti-rabbit IgG HRP (H + L) conjugate (W4021, Promega, IB: 1/4 000). Secondary antibodies for IF, from Jackson ImmunoResearch and diluted at 1/300 were: anti-mouse (711-165-151), anti-rabbit (711-165-152), anti-rat (711-166-150) Cy3; anti-mouse (711-175-150), anti-rabbit (711-175-152), anti-rat (711-175-153) Cy5; anti-mouse (715-546-150), anti-rabbit (711-545-152) Alexa Fluor 488; anti-mouse IgG1 Alexa 594 (115-585-205); anti-mouse IgG2b Alexa 488 (115-445-207). FITC-phalloidin (P5282, Sigma, IF:1/500) was used as a probe to label F-actin.

### siRNA-mediated depletion, transfection and exogenous expression of proteins

For siRNA-mediated depletion, 1 × $10^5$ cells were seed on glass coverslip or 12 mm Transwell filters (Corning Costar, #3460); or 3 × $10^5$ cells on 6-well plates. 24 hr post-seeding, cells were transfected for 8 hr with OptiMeM media (Gibco, #51985-026) containing Lipofectamine RNAiMAX (Invitrogen, #13778030) and 50 nM of either siControl, siγ-actin, siβ-actin, siNM2A or siNM2B (Supplementary Table 1). 3 days post-transfection, cells were fixed or lysed.

For transfections (rescue and exogenous expression experiments), 1 × $10^5$ cells were seed on glass coverslip or 12 mm Transwell filters; or 3 × $10^5$ cells on 6-well plates. 24 hr post-seeding, cells were transfected with either GFP or γ-actin using jetOPTIMUS DNA transfection reagent. Three days post-transfection cells were fixed or lysed. Levels of expression of the γ-actin transgene appeared low, as detected by IB (Supplementary Fig. 2e) because of the relatively low number of expressing cells. For FRAP experiments, 5 × $10^5$ MDCK were seed into glass-base dishes 27 mm (Thermo Fisher, #150682). 24 hr post-seeding, cells were transfected with either GFP-cingulin-FL or GFP-ZO-1-FL. Three days post-transfection, cells were imaged by FRAP.

### Immunoblot analysis

Confluent 10-cm dishes of cells were lysed for 10 min at 4 °C using 500 μL of RIPA buffer (150 mM NaCl, 40 mM Tris-HCl, 1% Triton X-100, 10% glycerol, 2 mM EDTA, 0.2% SDS, 0.5% deoxycholate, pH=7.5), supplemented with fresh protease inhibitor cocktail (PIC) (Thermo-Scientific, #A32965).

Cell lysates were sonicated (8 s at 66% amplitude using a Branson sonicator) and clarified by centrifugation at 15 700 g for 15 min at 4 °C. Protein concentration was quantified using the Pierce BCA Protein assay kit (ThermoScientific, #23225). 10 μg of protein samples were separated on 8% to 15% polyacrylamide gels and transferred to nitrocellulose membranes for 2 hr at 4 °C at 80 V. Membranes were then incubated with primary antibodies overnight at 4 °C, followed by incubation with secondary antibodies for 1 hr at RT. Protein detection was carried out using the WesternBright ECL kit (Advansta, #K12045-D50) and the Amersham ImageQuant 800 (Cytiva) imaging system. The signal intensity of proteins was quantified using Fiji/ImageJ version 2.16.0/1.54 g software. The relative signal intensity was expressed as a ratio between the signal of protein of interest and the signal of β-tubulin, which was used as a reference.

### Immunofluoresence analysis

For IF analysis, 1 ×$10^5$ cells were seeded on either glass coverslips or 12-mm Transwell filters. Cells were washed with PBS, fixed in 1% PFA at RT for 7 min for coverslips or 15 min for Transwell. The cells were then washed twice in PBS, incubated in methanol at -20 °C for 5 min for coverslips or 3 min for Transwell, followed by a gradual rehydration in PBS, and two washes in PBS. For Transwell, the filters were excised manually using a razor blade. Cells were permeabilized in 0.2% TritonX-100/PBS for 4 min at RT, and saturated in 2% BSA/PBS for 30 min at RT. Cells were incubated with primary antibodies at RT for 3 hr (in a humidified chamber), followed by three washes in PBS. Then, the cells were incubated with DAPI and secondary antibodies for 2 hr at RT, followed by three washes in PBS. The coverslips or filters were placed on glass slides with the cells facing up and mounted with Fluoromount-G. Slides were imaged on a Zeiss LSM800 confocal microscope using a

Plan-Apochromat 63x/1.40 oil objective at a resolution of 1024 × 1024 px. Maximum intensity projections of z-stack images were generated, typically 8-12 confocal planes with a step size of 0.21 μm. Image processing was performed using Fiji/ImageJ, including extraction from.czi files; and adjustment, cropping and assembly using Affinity Designer version 1.10.8.

To quantify junctional immunofluorescence, signal pixel intensity (mean gray value) for each channel was measured in the selected junctional area using the polyhedral tool of Fiji/ImageJ. The average background signal of the image was subtracted. Relative fluorescence intensity (RFI) was calculated as the ratio between the signal of the protein of interest and an internal junctional protein of reference (PLEKHA6 or PLEKHA7).

The zig-zag index (L(TJ)/L(St)) was measured as the ratio between the actual length of bicellular junction and the distance between two vertexes[33]. The length of the tight junction (L(TJ)) was measured by tracing a freehand line in Fiji/ImageJ, while the straight length of the junction (L(St)) was measured using a straight line between vertexes. Typically 90 junctions were analyzed for each condition for statistical analyses.

## qRT-PCR analysis

For qRT-PCR, 4 x $10^5$ cells were seeded in 6-well plates. On day 3, cells were washed with PBS, trypsinized, and centrifuged at 5000 g for 5 min. The supernatant was discarded, and RNA extraction was performed using the NucleoSpin® RNA kit (Macherey-Nagel, #740955.50). RNA concentration was measured using the SpectroStarNano spectrophotometer (BGM Labtech). The cDNA was synthesis from 1 μg of RNA using the iScript™ cDNA Synthesis kit (Bio-Rad, #1708890). cDNA concentration was measured using the SpectroStarNano spectrophotometer. qRT-PCR was performed on 20 ng of cDNA using the Master Mix Select SYBR™ kit (ThermoFisher Scientific, #4472908) and a CFX-connect thermocycler (BioRad). The following canis primers were used at 2.5 μM: HPRT (internal standard), forward 5′-TGGACAGGACTGAGCGGC-3′ and reverse 5′-TGAGCACACAGAGGGCTACG-3′; ACTB, forward 5′-AGCGCAAGTACTCTGTGTGG-3′ and reverse 5′-GTAACAGTCCGCCTAGAAGC-3′; MYH9, forward 5′-CTGCAAACTGGCCAAGGAGA-3′ and reverse 5′-GTCGGTGATCATCGCCTCAT-3′. The amplification conditions were: 2 min at 50 °C, followed by 2 min at 95 °C for, followed by 45 cycles of PCR amplification, each consisting of 95 °C for 15 sec and 58 °C for 1 min. Δ*Ct* values were obtained by subtracting the *Ct* value of the housekeeping gene HPRT from the *Ct* value for each of the indicated genes. ΔΔ*Ct* was calculated as the differences in Δ*Ct* between WT and γ-actin-KO (#2G3, #2H5, #3G9). Positive ΔΔ*Ct* values indicate more PCR cycles and therefore less mRNA. Conversely, negative ΔΔ*Ct* values indicate more mRNA. The fold changes were calculated −(ΔΔ*Ct*) by 2. For each experimental sample three replicates were performed.

## Measurement of transepithelial electrical resistance (TEER) and paracellular flux assay

To measure the TEER of MDCK monolayers at steady-state, 2 × $10^4$ cells were seeded in triplicate on 6.5 mm Transwell filters (Corning Costar, #3450). Cells were cultured in standard DMEM medium supplemented with FBS, NEAA, and P/S. The medium was changed every two days. On day 7, TER was measured, three measures per well, using the Millicell-ERS probe (Millipore) and the Millicell-ERS Volt-Ohm meter (Millipore).

To assess paracellular flux of 3 kDa fluorescein-dextran, 7 × $10^4$ cells were seeded in triplicate on 12 mm Transwell filters (Corning Costar, #3460). This medium was changed every two days. On day 7, TEER measurements were conducted to confirm cell confluency. Subsequently, cells were washed once with warm Hanks buffer (Gibco, #14025-050), and incubated for 30 min at 37 °C with fresh warm Hanks buffer. Then, cells were exposed to a 3 kDa fluorescein-dextran solution (Invitrogen, #D3305) at a concentration of 1 mg/mL in the apical compartment, while the basal compartment contained fresh Hanks buffer. After 1, 2, and 3 hr, 100 μL of the basal solution was collected and replaced with Hanks buffer. Fluorescence intensity was measured using a Cytation3 reader with excitation at 494 nm and emission at 521 nm. The permeability of 3 kDa fluorescein-dextran was calculated using the following formula:

$\mathrm{Perm}_{\mathrm{app}}$ = ([final 3 kDa fluorescein-dextran in basal compartment (ng/mL)] x $10^6$) / (filter area (1,12 $\mathrm{cm}^2$) x [initial 3 kDa fluorescein-dextran in apical compartment (ng/mL)] x time (s))[55].

## Atomic force microscopy (AFM) indentation measurements

AFM-based indentation measurements were conducted using a commercial AFM (Dimension FastScan, Icon Scanner, Bruker). A polystyrene bead with a radius of 5 μm (Invitrogen) was affixed onto a tipless silicon nitride cantilever (MLCT-O10-A, Bruker) using epoxy fixative. The spring constants of the custom-made cantilevers, calibrated prior to each measurement using the thermal fluctuation method, ranged from 0.025 to 0.14 N $\mathrm{m}^{-1}$.

All AFM indentation measurements were performed in cell culture medium at RT. Cells were cultured in 60 mm petri dishes for 36 hr in an incubator until they formed monolayers with confluency exceeding 80%. In a typical experiment, the cantilever was moved towards the cell layer at a constant speed of 1 μm $\mathrm{s}^{-1}$ until it reached a maximum contact force of 30 nN, corresponding to a maximum indentation distance of cells ranging up to 1.2 μm. Subsequently, the cantilever was retracted and relocated to another spot for the next cycle. A box pattern containing 50-100 spots within a 40 μm × 40 μm region was defined, with typically 10-20 such regions randomly selected for each measurement to determine the average stiffness of the cell.

The force-indentation traces were analyzed to derive the Young's modulus of the cells using the NanoScope Analysis program. Following baseline correction and contact point estimation, the approaching force-indentation curve was fitted with the Hertz (Spherical) model (Eq. 1) within the contact force range of 0.5 nN to 4.5 nN. Constant parameters and data range were selected to minimize bias across different cell types.

The Hertz (Spherical) model equation utilized for the fitting process is as follows[79]:

$$F = \frac{4E}{3(1-\upsilon^2)}\sqrt{R}\delta^{\frac{2}{3}} \tag{1}$$

where F represents the force exerted by the cantilever, δ denotes the indentation distance of the cell pressed by the cantilever, E signifies the Young's modulus of the cell layer, R represents the radius of the spherical indenter, and ν represents the Poisson ratio. The Poisson ratio of cells typically falls within the range of 0.3-0.5, and for all calculations, we adopted ν = 0.5[30].

For comparison of between γ-actin-KO and cingulin-KO MDCK cells, cells were seeded onto Petri dishes (μ-Dish; ibidi, Gräfelfing, Germany) and grown to confluence. The cell culture medium was exchanged by P/S (0.1 mg/mL; Biochrom) and HEPES (15 mM; Biochrom) containing medium. The AFM setup consists of a NanoWizard XP or NanoWizard 4 AFM (Bruker Nano, Berlin, Germany) mounted on top of an inverted optical microscope (IX81; Olympus). A Petri dish heater (Bruker Nano) keeps the sample at 37 °C during the measurement. Triangular cantilevers CP-PNPL-SiO-A (s-Qube, NanoandMore, USA equipped with colloidal probes (2 μm diameter) and a nominal force constant of 0.08 N/m were used after thermal calibration. Force relaxation experiments were conducted on cells to measure the viscoelastic response. In these experiments, cells are initially deformed up to a specific yield force of about 1 nN at which the feedback is switched to constant distance and force relaxation is monitored as a function of time. The indentation velocity was set to 2 μm/s. Once this yield force is reached, the indentation depth remains constant, and force relaxation is monitored. For this purpose, a distinct region of the cell culture sample of 5 × 5 µm$^2$ was indented as a squared grid of 8 × 8 px at the center referred to as force mapping.

### Viscoelasticity assessment

The theory used to fit the experimental force relaxation data is based on the central assumption that the plasma membrane/cortex shell resists deformation only by its tension $T$, which contains the prestress $T_0$ of the contractile actomyosin cortex and the area compressibility modulus times the relative area dilatation $K_A\alpha$:

$$T = T_0 + K_A\alpha. \tag{2}$$

$T_0$ is the time invariant prestress of the membrane/cortex shell, while the area compressibility modulus. $K_A$ reflects the elastic resistance to area strain. Viscoelasticity of $K_A$ is assumed to obey a power law $K_A = K_A^0\left(\frac{t}{t_0}\right)^{-\beta}$ with $0 \le \beta \le 1$ and $t_0 = 1\mathrm{s}$ (set arbitrarily). Application of the elastic-viscoelastic-correspondence principle gives:

$$T(t) = \mathrm{T} + \int_0^t K_A^0\left(\frac{t-\tau}{t_0}\right)^{-\beta}\frac{\partial\alpha(\tau)}{\partial\tau}\,\mathrm{d}\tau \tag{3}$$

The shape of the cell is assumed to be a spherical cap parameterized by a base radius and contact angle. Using this cap-like geometry as the starting point, the minimal surface is computed for various indentation depths and used to compute the force response as outlined previously[35].

### Isolation and analysis of apical cell cortices

The sandwich cleavage method[36] was used to obtain apical cell cortices from intact, living MDCK cells. WT and γ-actin-KO MDCK cells were seeded in 6-well tissue culture plates (TPP®) and grown to confluence. Glass coverslips (1.5H, 22 ×22 mm$^2$; Carl Roth GmbH) were washed twice alternately with water and ethanol followed by thorough cleaning in an oxygen plasma with a plasma cleaner (Zepto, Diener Electronics, Ebhausen, Germany). The glass coverslips were then incubated with the positively charged polymer poly-D-lysine (PDL, 0.2 g/L; Sigma-Aldrich) for 3 hr and rinsed once with distilled water. Subsequently, coated glass coverslips were placed on an osmotically swollen confluent MDCK cell monolayer, incubated for 30 min, and pulled off. After cleavage, isolated apical cell cortices were fixed in paraformaldehyde (PFA, 4% (w/v) in PBS) for 20 min and F-actin staining was performed by diluting Alexa FluorTM 488-phalloidin (6.6 µM) 1:40 in blocking/dilution buffer (1% (w/v) BSA in PBS) followed by incubation at RT for 45 min. The samples were rinsed twice with PBS after each step. On a microscope slide (76 ×26 mm, Epredia), the coverslip containing the isolated cell fragments was embedded in Mowiol (Carl Roth GmbH).

STED imaging was performed with an Abberior Expert line setup (Abberior Instruments) using an IX83 microscope (Olympus) with a 100x/1.40 oil immersion objective (UPLSAPO, Olympus). Alexa FlourTM 488 was excited with a 485 nm excitation laser (20% of maximum power) and detected with a 525 - 575 nm avalanche photodiode (APD). The depletion laser was a 595 nm pulsed solid-state laser (set to ~5% of the maximum power of 2 W). For all STED images, the pixel size was 20 nm with a dwell time of 2.5 µs per pixel, a line averaging of 6 at a resolution of 1000 × 1000 px$^2$. Sections of 400 × 400 px$^2$ were selected from the resulting STED images for image analysis.

### Fluorescence Recovery After Photobleaching (FRAP)

For FRAP experiments, MDCK cells were transfected with constructs coding for either GFP-cingulin-FL or GFP-ZO-1-FL and were cultured into glass-base dishes 27 mm (Thermo Fisher, #150682) for 72 hr in normal culture medium (DMEM + 10% FBS + 1% P/S). FRAP assay were performed in HBSS containing 15 mM Hepes pH: 7,4 in a temperature-controlled stage (37°C) on a Leica SP8 or a Leica Stellaris8 confocal microscopes using a X63 immersive objective. For blebbistatin treatment, either blebbistatin (Sigma, #B0560) or DMSO (control condition) were added at final concentration of 50 µM for 3 hr before the experiment in normal medium, and added at the same concentration to the HBSS medium for the experiment.

Five images were acquired every 1:290 s before photobleaching. Cell-cell junctions were photobleached four times during 1:280 s at 70%, and images were acquired at regular intervals for a recovery period of 10 min. The first 2 min post-bleach, images were acquired every 2 s, and the last 8 min of acquisition images were each 5 s. Using Fiji/ImageJ version 2.16.0/1.54 g, the rate of photobleaching was calculated by comparing the fluorescence of the control region before (Fc0) and after (Fc) photobleaching (r=Fc/Fc0). The fluorescence intensity was normalized by subtracting the background region intensity (Fb) to the junctional region of interest intensity (Fj), all divided by the rate of photobleaching (F = (Fj-Fb)/r). The mobile fraction and half-time (t1/2) were calculated by fitting a one-phase decay nonlinear regression using GraphPad Prism version 10.4.1[80].

### Quantification and Statistical analysis

GraphPad Prism version 10.4.1 software was used for data processing and analysis. All experiments were conducted at least in triplicate. Data are presented as dot-plots, histograms or line-graphs with mean values and standard deviations (SD) indicated to represent the variability. Nested analysis was conducted to identify outliers. Any detected outliers were excluded from the statistical analysis. Statistical significance was determined using either a one-way Anova two-sided test, preceded by verifying the normal distribution using Kolmogovor-Smirnov test, or an unpaired Mann-Whitney two-sided test (when comparing two sets of data). The p-value from the test was directly incorporated into the figure.

### Reporting summary

Further information on research design is available in the Nature Portfolio Reporting Summary linked to this article.

## Data availability

The raw images from immunofluorescence experiments generated in this study have been deposited in the FigShare database [https://doi.org/10.6084/m9.figshare.28309337][81]. Source data are provided with this paper.

## References

1. Bruckner, B. R. & Janshoff, A. Elastic properties of epithelial cells probed by atomic force microscopy. *Biochim. Biophys. Acta* **1853**, 3075–3082 (2015).
2. Yap A. S., Duszyc K., Viasnoff V. Mechanosensing and Mechanotransduction at Cell-Cell Junctions. *Cold Spring Harb Perspect Biol*. (2017).
3. Citi, S. The mechanobiology of tight junctions. *Biophys. Rev.* **11**, 783–793 (2019).
4. Pinheiro, D. & Bellaiche, Y. Mechanical Force-Driven Adherens Junction Remodeling and Epithelial Dynamics. *Dev. Cell* **47**, 3–19 (2018).
5. Pelaseyed, T. & Bretscher, A. Regulation of actin-based apical structures on epithelial cells. *J. Cell Sci.* **131**, jcs221853 (2018).
6. Morales, E. A., Gaeta, I. & Tyska, M. J. Building the brush border, one microvillus at a time. *Curr. Opin. Cell Biol.* **80**, 102153 (2023).
7. Park, J. & Bird, J. E. The actin cytoskeleton in hair bundle development and hearing loss. *Hear. Res.* **436**, 108817 (2023).
8. Vedula, P. & Kashina, A. The makings of the 'actin code': regulation of actin's biological function at the amino acid and nucleotide level. *J. Cell Sci.* **131**, jcs215509 (2018).

9. Ivanov, A. I., Lechuga, S., Marino-Melendez, A. & Naydenov, N. G. Unique and redundant functions of cytoplasmic actins and non-muscle myosin II isoforms at epithelial junctions. *Ann. N. Y Acad. Sci.* **1515**, 61–74 (2022).
10. Perrin, B. J. & Ervasti, J. M. The actin gene family: function follows isoform. *Cytoskeleton (Hoboken)* **67**, 630–634 (2010).
11. Dugina, V. B., Shagieva, G. S. & Kopnin, P. B. Biological Role of Actin Isoforms in Mammalian Cells. *Biochemistry (Mosc)* **84**, 583–592 (2019).
12. Dugina, V., Zwaenepoel, I., Gabbiani, G., Clement, S. & Chaponnier, C. Beta and gamma-cytoplasmic actins display distinct distribution and functional diversity. *J. Cell Sci.* **122**, 2980–2988 (2009).
13. Baranwal, S. et al. Nonredundant roles of cytoplasmic beta- and gamma-actin isoforms in regulation of epithelial apical junctions. *Mol. Biol. Cell* **23**, 3542–3553 (2012).
14. Pasquier, E. et al. gamma-Actin plays a key role in endothelial cell motility and neovessel maintenance. *Vasc. Cell* **7**, 2 (2015).
15. Malek, N. et al. Knockout of ACTB and ACTG1 with CRISPR/Cas9(D10A) Technique Shows that Non-Muscle beta and gamma Actin Are Not Equal in Relation to Human Melanoma Cells' Motility and Focal Adhesion Formation. *Int J. Mol. Sci.* **21**, 2746 (2020).
16. Lechuga, S. et al. Loss of beta-Cytoplasmic Actin in the Intestinal Epithelium Increases Gut Barrier Permeability in vivo and Exaggerates the Severity of Experimental Colitis. *Front Cell Dev. Biol.* **8**, 588836 (2020).
17. Belyantseva, I. A. et al. Gamma-actin is required for cytoskeletal maintenance but not development. *Proc. Natl. Acad. Sci. USA* **106**, 9703–9708 (2009).
18. Bunnell, T. M. & Ervasti, J. M. Delayed embryonic development and impaired cell growth and survival in Actg1 null mice. *Cytoskeleton (Hoboken)* **67**, 564–572 (2010).
19. Perrin, B. J., Sonnemann, K. J. & Ervasti, J. M. beta-actin and gamma-actin are each dispensable for auditory hair cell development but required for Stereocilia maintenance. *PLoS Genet.* **6**, e1001158 (2010).
20. Bruckner, B. R. & Janshoff, A. Importance of integrity of cell-cell junctions for the mechanics of confluent MDCK II cells. *Sci. Rep.* **8**, 14117 (2018).
21. Tang, V. W. Cell-cell adhesion interface: orthogonal and parallel forces from contraction, protrusion, and retraction. *F1000Res.* **7**, F1000 Faculty Rev-1544 (2018).
22. Dugina, V. B., Shagieva, G. S. & Kopnin, P. B. Cytoplasmic Beta and Gamma Actin Isoforms Reorganization and Regulation in Tumor Cells in Culture and Tissue. *Front Pharm.* **13**, 895703 (2022).
23. Nietmann, P. et al. Cytosolic actin isoforms form networks with different rheological properties that indicate specific biological function. *Nat. Commun.* **14**, 7989 (2023).
24. Conti, M. A. & Adelstein, R. S. Nonmuscle myosin II moves in new directions. *J. Cell Sci.* **121**, 11–18 (2008).
25. Vicente-Manzanares, M., Ma, X., Adelstein, R. S. & Horwitz, A. R. Non-muscle myosin II takes centre stage in cell adhesion and migration. *Nat. Rev. Mol. Cell Biol.* **10**, 778–790 (2009).
26. Chinthalapudi, K. & Heissler, S. M. Structure, regulation, and mechanisms of nonmuscle myosin-2. *Cell Mol. Life Sci.* **81**, 263 (2024).
27. Ma, X. et al. Ablation of nonmuscle myosin II-B and II-C reveals a role for nonmuscle myosin II in cardiac myocyte karyokinesis. *Mol. Biol. Cell* **21**, 3952–3962 (2010).
28. Efimova, N. & Svitkina, T. M. Branched actin networks push against each other at adherens junctions to maintain cell-cell adhesion. *J. Cell Biol.* **217**, 1827–1845 (2018).
29. Heuze, M. L. et al. Myosin II isoforms play distinct roles in adherens junction biogenesis. *Elife* **8**, e46599 (2019).
30. Rouaud, F. et al. Cingulin and paracingulin tether myosins-2 to junctions to mechanoregulate the plasma membrane. *J. Cell Biol.* **322**, e202208065 (2023).
31. Smutny, M. et al. Myosin II isoforms identify distinct functional modules that support integrity of the epithelial zonula adherens. *Nat. Cell Biol.* **12**, 696–702 (2010).
32. Dugina, V., Shagieva, G., Khromova, N. & Kopnin, P. Divergent impact of actin isoforms on cell cycle regulation. *Cell Cycle* **17**, 2610–2621 (2018).
33. Tokuda, S., Higashi, T. & Furuse, M. ZO-1 Knockout by TALEN-Mediated Gene Targeting in MDCK Cells: Involvement of ZO-1 in the Regulation of Cytoskeleton and Cell Shape. *PLoS One* **9**, e104994 (2014).
34. Cordes, A. et al. Prestress and Area Compressibility of Actin Cortices Determine the Viscoelastic Response of Living Cells. *Phys. Rev. Lett.* **125**, 068101 (2020).
35. Nietmann, P. et al. Epithelial cells fluidize upon adhesion but display mechanical homeostasis in the adherent state. *Biophys. J.* **121**, 361–373 (2022).
36. Hubrich, H. et al. Viscoelasticity of Native and Artificial Actin Cortices Assessed by Nanoindentation Experiments. *Nano Lett.* **20**, 6329–6335 (2020).
37. Noding, H. et al. Rheology of Membrane-Attached Minimal Actin Cortices. *J. Phys. Chem. B* **122**, 4537–4545 (2018).
38. Shen, L., Weber, C. R. & Turner, J. R. The tight junction protein complex undergoes rapid and continuous molecular remodeling at steady state. *J. Cell Biol.* **181**, 683–695 (2008).
39. Yu, D. et al. MLCK-dependent exchange and actin binding region-dependent anchoring of ZO-1 regulate tight junction barrier function. *Proc. Natl. Acad. Sci. USA* **107**, 8237–8241 (2010).
40. Paschoud, S. et al. Cingulin and paracingulin show similar dynamic behaviour, but are recruited independently to junctions. *Mol. Membr. Biol.* **28**, 123–135 (2011).
41. Leavitt, J. et al. Expression of transfected mutant beta-actin genes: alterations of cell morphology and evidence for autoregulation in actin pools. *Mol. Cell Biol.* **7**, 2457–2466 (1987).
42. Ng, S. Y., Erba, H., Latter, G., Kedes, L. & Leavitt, J. Modulation of microfilament protein composition by transfected cytoskeletal actin genes. *Mol. Cell Biol.* **8**, 1790–1794 (1988).
43. Lloyd, C., Schevzov, G. & Gunning, P. Transfection of nonmuscle beta- and gamma-actin genes into myoblasts elicits different feedback regulatory responses from endogenous actin genes. *J. Cell Biol.* **117**, 787–797 (1992).
44. Miralles, F., Posern, G., Zaromytidou, A. I. & Treisman, R. Actin dynamics control SRF activity by regulation of its coactivator MAL. *Cell* **113**, 329–342 (2003).
45. Halder, G., Dupont, S. & Piccolo, S. Transduction of mechanical and cytoskeletal cues by YAP and TAZ. *Nat. Rev. Mol. Cell Biol.* **13**, 591–600 (2012).
46. Dupont, S. et al. Role of YAP/TAZ in mechanotransduction. *Nature* **474**, 179–183 (2011).
47. Gerber, A. et al. Blood-borne circadian signal stimulates daily oscillations in actin dynamics and SRF activity. *Cell* **152**, 492–503 (2013).
48. Olson, E. N. & Nordheim, A. Linking actin dynamics and gene transcription to drive cellular motile functions. *Nat. Rev. Mol. Cell Biol.* **11**, 353–365 (2010).
49. Panciera, T., Azzolin, L., Cordenonsi, M. & Piccolo, S. Mechanobiology of YAP and TAZ in physiology and disease. *Nat. Rev. Mol. Cell Biol.* **18**, 758–770 (2017).
50. Lechuga, S. et al. Loss of gamma-cytoplasmic actin triggers myofibroblast transition of human epithelial cells. *Mol. Biol. Cell* **25**, 3133–3146 (2014).
51. Wiggan O., & Stasevich T. J. Single molecule imaging of the central dogma reveals myosin-2A gene expression is regulated by contextual translational buffering. *bioRxiv*, (2024).
52. Bergeron, S. E., Zhu, M., Thiem, S. M., Friderici, K. H. & Rubenstein, P. A. Ion-dependent polymerization differences between mammalian beta- and gamma-nonmuscle actin isoforms. *J. Biol. Chem.* **285**, 16087–16095 (2010).

53. Muller, M. et al. Distinct functional interactions between actin isoforms and nonsarcomeric myosins. *PLoS One* **8**, e70636 (2013).
54. Citi, S. et al. A short guide to the tight junction. *J. Cell Sci.* **137**, jcs261776 (2024).
55. Van Itallie, C. M., Fanning, A. S., Bridges, A. & Anderson, J. M. ZO-1 stabilizes the tight junction solute barrier through coupling to the perijunctional cytoskeleton. *Mol. Biol. Cell* **20**, 3930–3940 (2009).
56. Hildebrand, J. D. Shroom regulates epithelial cell shape via the apical positioning of an actomyosin network. *J. Cell Sci.* **118**, 5191–5203 (2005).
57. Nakajima, H. & Tanoue, T. Lulu2 regulates the circumferential actomyosin tensile system in epithelial cells through p114RhoGEF. *J. Cell Biol.* **195**, 245–261 (2011).
58. Lynn, K. S., Peterson, R. J. & Koval, M. Ruffles and spikes: Control of tight junction morphology and permeability by claudins. *Biochim Biophys. Acta Biomembr.* **1862**, 183339 (2020).
59. Pinto-Duenas D. C. et al. The Role of ZO-2 in Modulating JAM-A and gamma-Actin Junctional Recruitment, Apical Membrane and Tight Junction Tension, and Cell Response to Substrate Stiffness and Topography. *Int. J. Mol. Sci.* **25**, (2024).
60. Zhu, M. et al. Mutations in the gamma-actin gene (ACTG1) are associated with dominant progressive deafness (DFNA20/26). *Am. J. Hum. Genet.* **73**, 1082–1091 (2003).
61. Zhu, G. J. et al. Cingulin regulates hair cell cuticular plate morphology and is required for hearing in human and mouse. *EMBO Mol. Med.* **15**, e17611 (2023).
62. Walsh, T. et al. Genomic duplication and overexpression of TJP2/ZO-2 leads to altered expression of apoptosis genes in progressive nonsyndromic hearing loss DFNA51. *Am. J. Hum. Genet.* **87**, 101–109 (2010).
63. Ben-Yosef, T. et al. Claudin 14 knockout mice, a model for autosomal recessive deafness DFNB29, are deaf due to cochlear hair cell degeneration. *Hum. Mol. Genet.* **12**, 2049–2061 (2003).
64. Gow, A. et al. Deafness in Claudin 11-null mice reveals the critical contribution of basal cell tight junctions to stria vascularis function. *J. Neurosci.* **24**, 7051–7062 (2004).
65. Nayak, G. et al. Tricellulin deficiency affects tight junction architecture and cochlear hair cells. *J. Clin. Invest* **123**, 4036–4049 (2013).
66. Kitajiri, S. et al. Deafness in occludin-deficient mice with dislocation of tricellulin and progressive apoptosis of the hair cells. *Biol. open* **3**, 759–766 (2014).
67. Guillemot, L. et al. Disruption of the cingulin gene does not prevent tight junction formation but alters gene expression. *J. cell Sci.* **117**, 5245–5256 (2004).
68. Guillemot, L. et al. Cingulin is dispensable for epithelial barrier function and tight junction structure, and plays a role in the control of claudin-2 expression and response to duodenal mucosa injury. *J. Cell Sci.* **125**, 5005–5012 (2012).
69. Mauperin M., Sassi A., Mean I., Feraille E., & Citi S. Knock Out of CGN and CGNL1 in MDCK Cells Affects Claudin-2 but Has a Minor Impact on Tight Junction Barrier Function. *Cells* **12**, (2023).
70. Vasileva, E. et al. Cingulin binds to the ZU5 domain of scaffolding protein ZO-1 to promote its extended conformation, stabilization, and tight junction accumulation. *J. Biol. Chem.* **298**, 101797 (2022).
71. Fanning, A. S., Jameson, B. J., Jesaitis, L. A. & Anderson, J. M. The Tight Junction Protein ZO-1 Establishes a Link between the Transmembrane Protein Occludin and the Actin Cytoskeleton. *J. Biol. Chem.* **273**, 29745–29753 (1998).
72. Wittchen, E. S., Haskins, J. & Stevenson, B. R. Protein interactions at the tight junction. Actin has multiple binding partners, and ZO-1 forms independent complexes with ZO-2 and ZO-3. *J. Biol. Chem.* **274**, 35179–35185 (1999).
73. Belardi, B. et al. A Weak Link with Actin Organizes Tight Junctions to Control Epithelial Permeability. *Dev. Cell* **54**, 792–804.e797 (2020).
74. D'Atri, F. & Citi, S. Cingulin interacts with F-actin in vitro. *FEBS Lett.* **507**, 21–24 (2001).
75. Paschoud, S. & Citi, S. Inducible overexpression of cingulin in stably transfected MDCK cells does not affect tight junction organization and gene expression. *Mol. Membr. Biol.* **25**, 1–13 (2008).
76. Paschoud, S., Jond, L., Guerrera, D. & Citi, S. PLEKHA7 modulates epithelial tight junction barrier function. *Tissue barriers* **2**, e28755 (2014).
77. Ballestrem, C., Wehrle-Haller, B. & Imhof, B. A. Actin dynamics in living mammalian cells. *J. Cell Sci.* **111**, 1649–1658 (1998).
78. Sluysmans, S. et al. PLEKHA5, PLEKHA6 and PLEKHA7 bind to PDZD11 to target the Menkes ATPase ATP7A to the cell periphery and regulate copper homeostasis. *Mol. Biol. Cell* **32**, 1–20 (2021).
79. Harris, A. R. & Charras, G. T. Experimental validation of atomic force microscopy-based cell elasticity measurements. *Nanotechnology* **22**, 345102 (2011).
80. Zheng C. Y., Petralia R. S., Wang Y. X., Kachar B. Fluorescence recovery after photobleaching (FRAP) of fluorescence tagged proteins in dendritic spines of cultured hippocampal neurons. *J. Vis. Exp.* (2011).
81. Mauperin M., et al. A feedback circuitry involving gamma-actin, beta-actin and non-muscle myosin 2A controls tight junction and apical cortex mechanics. figshare. Dataset. *Nat. Commun.* https://doi.org/10.6084/m9.figshare.28309337 (2025).

## Acknowledgements

SC is funded by the Swiss National Fund for Scientific Research (grant n. 310030_200681) and the State of Geneva. Y.S. and J. Y. are funded by the Singapore Ministry of Education Academic Research through the MOE Research Scholarship Block (RSB) scheme (to Y. S.) and the Singapore Ministry of Education under the Research Centres of Excellence program (to J. Y.). A.J. is funded by the German Federal Ministry of Education and Research (BMBF), the Max Planck Society and the Deutsche Forschungsgemeinschaft (022379, EXC 2067-390729940). A.J. and N.K. gratefully acknowledge financial support from RTG2756 (B01).

## Author contributions

Conceptualization, S.C., M.M., Y.S., J.Y., A.J.; Methodology, M.M., Y.S., T.G., T.A.O., N.K, B.G., I.M., A.M-M., L.J. and S.C; Validation, M.M., Y.S. and S.C.; Investigation, M.M., Y.S., T.G., T.A.O., N.K, B.G., I.M., A.M-M., L.J., J.Y., A.J.and S.C; Resources, M.M., Y.S., I.M., A.M-M., L.J., J.Y. and S.C.; Data Curation, M.M., Y.S.; Writing – Original Draft, S.C., M.M.; Writing – Review & Editing, S.C., M.M.; Visualization, S.C., M.M.; Supervision, S.C., J. Y., A.J.; Project Administration, S.C.; Funding Acquisition, S.C., J. Y., A.J.

## Competing interests

The authors declare no competing interest.

## Additional information

**Supplementary information** The online version contains supplementary material available at https://doi.org/10.1038/s41467-025-57428-y.

**Correspondence** and requests for materials should be addressed to Sandra Citi.

**Peer review information** *Nature Communications* thanks the anonymous reviewers for their contribution to the peer review of this work. A peer review file is available.